Suspension high velocity oxy-fuel spraying of TiO_2: A quantitative approach to phase composition

Z. Pala[1], E. Shaw[1], J.W. Murray[1], N. Senin[1], T. Hussain[1*]

[1]Faculty of Engineering, University of Nottingham, University Park, Nottingham NG7 2 RD, UK

*to whom correspondence should be addressed; tel.: +440 1158413795; e-mail: tanvir.hussain@nottingham.ac.uk

Abstract

A range of coatings from water suspension of anatase has been prepared by suspension high velocity oxy-fuel spraying with the aim to study effects of heat power of the flame on phase composition, microstructure and surface topography. Three most commonly used approaches of quantitative phase analysis have been scrutinized with respect to their applicability and as some of the coatings showed presence of preferred orientation it was argued that quantitative Rietveld refinement is the most accurate method for phase composition determination. Coatings had a layered duplex anatase/rutile microstructure with fraction of rutile increasing exponentially with heat power. Spraying at the lower heat power led to a lower surface roughness and higher power resulted in surfaces with pronounced humps, which were distributed homogeneously on the surface. The emergence of humps is related to an increase in macroscopic surface area of up to 30 % with respect to the flat coating.

Key words: suspension HVOF spraying, Rietveld refinement, topography, anatase, rutile

1. Introduction

Thermal spraying of powders dispersed in suspension, most often ethanol or water, has facilitated deposition of nanosized particles [1] and thus, production of coatings with novel structure, microstructure and properties. The contributions of this technique towards production of coatings with low thermal conductivities [2], unique microstructural features such as high specific surface area [3] or simply thin coatings to bridge the gap between traditional thin film and conventional thermal sprayed

coatings have already been demonstrated. There are still many opportunities for further expansion of suspension based thermal sprayed coatings and to understand the relationships between processing parameters and microstructure [4].

Suspensions of oxide ceramics such as alumina, zirconia and titania have been widely sprayed employing both plasma jets and HVOF techniques. Owing to titania being the favourite photocatalytic material [5], suspension sprayed titania have been investigated from the viewpoint of different suspension injectors [6], spray distance [7], coating hardness [8] and tribological behaviour of the coating [9]. One of the main factors which was studied and taken into consideration was the phase transformation between the two titania phases of anatase and rutile, and more rarely also brookite and titania suboxides. When anatase powder and/or suspension is deposited, it is reasonable to expect both transformation into rutile during thermal spraying due to the fact that it is the more stable phase [10] and the preservation of anatase, likely due to its less constrained molecular structure in comparison to rutile. Traditionally, titanium dioxide is a prime semiconductor photooxidative catalyst material and anatase has been generally considered to exhibit higher photocatalytic activity [11] and thus tunability of anatase/rutile ratio has been of prime interest [12]. However, it was shown a decade ago that multiphase TiO_2 with addition of rutile [13] and/or brookite [14] or even a rutile/brookite mixture [15] can possess better photocatalytic properties than pure anatase mainly due to phenomena connected with electron and hole transfer between the phases. Furthermore, rutile-rich titania is considered as a better choice for sonophotocatalytic reaction of water (see e.g. page 211 in [16]) embodying another important application area aside from the self-cleaning and self-sterilizing surfaces [17]. Moreover, in the transformation from tetragonal anatase of the $I4_1/amd$ space group into tetragonal rutile with $P4_2/mnm$ space group (more on differences between these two crystal structures can be found e.g. in a review by Linsebigler et al. [18]), oxygen vacancies play a prominent role by promoting the transformation and lack of oxygen leading, under certain conditions [19], in creation of the nonstoichiometric Andersson-Magnéli titania phases [20] which have been singled out as promising thermoelectric materials [21].

Among the methods employed for titania coatings quantitative composition of constituent phases, powder X-ray diffraction (PXRD) has had a prominent place. However, computation of quantities from PXRD pattern is not a straightforward task and traditionally phenomenological

approaches [22] [23] have been used for quantification of phases in thermally sprayed coatings and even in sol-gel prepared powders [24]. Such approaches usually take into account only selected reflections and not the entire measured spectrum, which lead to erroneous results when crystallographic texture or nanosized phases are present in the irradiated volume. Texture, or preferred orientation, cannot be ruled out in thermally sprayed coatings due to inherent directionality and, hence, anisotropy of the deposition process. Specifically for titania, it was reported that plasma spraying led to textured titania coatings [25].

Besides phase composition there are three other crucial parameters which determine the photocatalytic and/or sonophotocatalytic activity of TiO_2, namely the presence of defects, surface area [26] and crystallite size [27]. Surface area of powder materials is commonly assessed by specific surface area defined as total area to mass of the solid sample and principles of Brunnauer-Emmett-Teller theory [28] are used for its measurement. When the effect of specific surface area on the (sono)photocatalytic activity of TiO_2 is investigated, Langmuir-Hinshelwood behaviour [29] is often reported for the rate of photocatalytic reactions [30] and, thus, linear dependence of mass of the adsorbent on the photocatalyst surface (page 30 in [16]) is expected. Effectively, larger specific surface area leads to higher photocatalytic activity. At the same time, there is a correlation between smaller crystallite size and higher photocatalytic activity [27]. For coatings, (sono)photocatalysis takes place on the surface exposed to the outer environment and any maximization of exposed surface area is beneficial, analogically to powders. Furthermore, the ability to spray finer particles in suspension thermal spraying processes will contribute to obtaining a coating with smaller crystallite sizes.

The aim of this study was to investigate the phase composition quantitatively as a function of processing parameters. Since it has been established that the rate at which rutile transforms to anatase is an exponential function of temperature [10], we have investigated the effects of heat power onto the anatase/rutile ratio in coatings determined by quantitative Rietveld refinement [31] employing principles of Hill and Howard [32] and a whole powder pattern modelling approach [33] to refinement of crystallite sizes and microstrain values. The impact of processing parameters on the outer surface area of the coating is established from analysis of surface topography data.

2. Experimental

2.1. Materials

A commercially available 20 wt.% water based anatase suspension (D50 = 180 nm, Millidyne, Finland) was used in this study. Laser diffractometry data (Beckman Coulter laser diffractometer) provided by the supplier showed a bimodal size distribution with one range between 10 - 500 nm with a median of ~180 nm and another range between 1- 10 µm with a median of ~5 µm. The larger size distribution was due to formation of agglomerates in the manufacturing process (i.e., additives to stabilise the suspension). The suspension was sprayed onto stainless steel substrates of dimensions 60×25×2 mm^3. The AISI 304 stainless steel had a nominal composition of Fe-19.0Cr- 9.3 Ni- 0.05 C (in wt.%).

2.2. Sample manufacturing

The samples were grit-blasted using F100 brown alumina with size range from 0.125 to 0.149 mm, cleaned in an ultrasonic bath to remove any embedded alumina particles and finally, cleaned in acetone. The samples were then mounted onto a carousel rotating at 73 rpm with a vertical axis of rotation. The rotation speed was set to impart a surface velocity to the substrates of approximately 1 m/s across the spray path. A modified UTP/ Miller Thermal High Velocity Oxy Fuel (HVOF) system with a direct injection at the centre of the gas mixing block was used to spray the suspension. The Suspension High Velocity Oxy Fuel (SHVOF) setup has a modified mixing block and a modified gun back body without any modification to the combustion chamber and the nozzle. The suspension injector had a diameter of 0.3 mm to inject the suspension into the centre of the combustion chamber. A 22 mm long combustion chamber with 110 mm long barrel nozzle was used in this study. The suspension was fed using a pressurised 2 litre vessel equipped with a mechanical stirrer after being homogenised before spraying for 90 minutes using a mechanical stirring system. The pressure of the feeding system was fixed at 3 bar during the spray giving a flow rate of ~80 ml/min. At the end of each spray run de-ionised water was supplied to clean the nozzle.

The gun was mounted on a z-axis traverse unit in front of the rotating carousel and it was set to a stand-off distance from the surface of the substrate of 85 mm. The gun was scanned vertically up and down at 5 mm/s to build up a coating of the required thickness. In all spray conditions, 10 spray passes

were used. During and after the spray run, compressed air jets were directed towards the substrates to provide cooling. Hydrogen was used as a combustion fuel and the flow rates were set using a volume control system for fuel gas and oxygen. The main reason for using hydrogen as fuel was that it results in the cleanest combustion products and the chance of carbon contamination in the coating is significantly reduced. Furthermore, a trace amount of contamination can have a large impact on photocatalytic behaviour in functional coatings.

There are a large number of processing variables in suspension HVOF spraying, and the present samples form a sub-set of a matrix of experiments, designed to identify the influence of process parameters on coating compositions. The hydrogen and oxygen flow rates during the spray are reported in Table 1. These were all sprayed at 100% oxygen stoichiometry, since the influence of excess oxygen in the flame on the oxide ceramic feedstock was not a main focus of our study. All the rest of the parameters were held constant during the spray runs. The theoretical flame energy for each spray condition was calculated using standard combustion formulae and the samples are labelled according to their theoretical flame energy values throughout the paper.

Table. 1 Gas flow rates and calculated heat power of the combustion flame.

Coating	**O_2 flow rate [l/min]**	**H_2 flow rate [l/min]**	**Total flow rate [l/min]**	**Flame heat power [kW]**
TG40	244	122	367	40
TG56	338	169	508	56
TG72	438	219	657	72
TG85	517	259	776	85
TG101	611	306	917	101

2.3. Coating characterization

An FEI XL30 (FEI Europe, Eindhoven, The Netherlands) SEM operated at 20 kV was used to investigate the feedstock suspension and coating microstructure in cross-section and on the as-sprayed surface. Secondary electron (SE) and backscattered electron (BSE) images were used to form images as required. The samples were sectioned transversely with a SiC slitting wheel in a precision cutting saw, mounted in conductive resin and ground and polished to 1 µm surface finish. Metallographic specimens were carbon coated prior to SEM investigations.

An Alicona Infinite Focus G5 (Alicona, Germany) areal topography measurement instrument based on focus-variation, optical technology was employed for scanning the coating top surface. Data were processed according to ISO 25178 [34] supplying the height parameters *Sp* (maximum height of peaks) and (arithmetical mean height of the surface). The analysis of height parameters was done for each coating in five areas, by using a 5× objective, with field of view: 2.82 mm × 2.82 mm, and sampling at 7.8 μm lateral resolution. Topography was filtered with 2 μm and 0.8 mm S and L nesting indices respectively (these are cut-off frequencies to remove high and low-frequency texture components, as detailed in ISO 25178). For a more detailed characterization of surface topography a finer resolution is needed, hence, we made five measurements in five different places on the coatings with a 50× objective (field of view 0.244 μm × 0.244 μm, and sampling at 2.1 μm lateral resolution. Topography was filtered with 0.5 μm and 80 μm *S* and *L* nesting indices respectively. In this configuration, the ISO 25178 hybrid parameter: developed interfacial area ratio *Sdr* was computed. The actual *Sdr* values are given in percentages, so that Sdr = 0% reflects a flat area while e.g. Sdr = 10% means that the gain in surface area is 10 % in respect to the ideal flat.

As-sprayed coatings were analysed by a D500 Siemens powder X-ray diffractometer in Bragg-Brentano θ-2θ geometry equipped with copper anode X-ray tube and a scintillation point detector. The 2θ range scanned by Cu*Kα* radiation was from 20º to 90º with 0.05º step size and 5 s of counting time in each step. Guidelines from [35] were meticulously followed both during measurement and during Rietveld refinement procedure which was carried out in TOPAS V5 software package. Considering the refinement, we aimed for determination of the following structural and microstructural parameters of both anatase and rutile: (i) lattice parameters *a* and *c*, (ii) quantities in wt.% according to Hill and Howard [32], (iii) average sizes of coherently scattering domains, i.e. average crystallite sizes, and (iv) microstrains. Crystallite sizes and microstrains were refined under the assumption that small crystallites contribute to Lorentzian broadening while the presence of microstrains, or 2nd order residual stresses, lead to Gaussian broadening [36]. The broadening was characterized by FWHM (Full Width at Half maximum) values rather than with integral breadths due to issues connected with general applicability of integral breadth methods in cases when effects of both the crystallite sizes and microstrains are expected [37]. In this manner, the entire measured 2θ range was used for determination of the above

mentioned parameters from PXRD patterns. The instrumental broadening was accounted for by employing a fundamental parameters approach [38] where the details of experimental set-up such as radiation source, slits, detector, etc. are used for instrumental function calculations instead of its direct determination by measuring sample without any physical broadening effects. The rutile and anatase quantities obtained from Rietveld refinement were compared to those computed following a rather simple approach, which has been somewhat dominant in the thermal spraying community dealing with titania materials. Using integral intensities of only (101) anatase ($I^{(101)A}$) and (110) rutile ($I^{(110)R}$) reflections, Berger-Keller et al. [22] obtain the anatase volume fraction with the formula:

$$C(anatase) = \frac{8 \cdot I^{(101)A}}{8 \cdot I^{(101)A} + 13 \cdot I^{(110)R}} \cdot 100\% \quad (1)$$

which was recalculated into weight fraction using 3.78 g/cm^3 and 4.23 g/cm^3 for densities of anatase and rutile respectively.

Eventually, since the two most widely used methods of quantitative phase analysis [39] are quantitative Rietveld refinement (QRR) and rather semi-quantitative Reference Intensity Ratios (RIR) method, we also computed phase quantities following a normalized RIR method [40] using star quality PDF entries for both phases, namely entries with reference code 21-1272 for anatase (RIR = 3.30) and 21-1276 for rutile (RIR = 3.40).

Since both the RIR approach and equation (1) assume random orientation of crystallite aggregates in the irradiated volume, Lotgering factor *F(hkl)* [41] was computed for the three theoretically most intensive rutile reflections of (110), (101) and (211). The Lotgering factor represents a simple qualitative measure to assess whether any preferred orientation in the irradiated volume is present by comparing peak or integral intensities of the measured PXRD pattern and those of a randomly oriented powder sample. Instead of powder sample, relative intensities from PDF entries can be used. The comparison is made for the intensity of selected (hkl) (I^{hkl}) and the intensities I in a chosen 2θ range in the following manner:

$$F(hkl) = \frac{\frac{I^{hkl}}{\sum_{2\theta\ range} I} - \frac{I_0^{hkl}}{\sum_{2\theta\ range} I_0}}{1 - \frac{I_0^{hkl}}{\sum_{2\theta\ range} I_0}} \quad (2)$$

where *0* denotes the intensities of samples with random orientations, either measured or from PDF entries. Lotgering factor of 0 corresponds to a completely random distribution while the value of 1 would indicate a complete orientation of the chosen (hkl) planes in the sample. Due to overlap of anatase and rutile reflections in measured PXRD patterns, Lotgering factor was computed using peak intensity values after background level subtraction of the measured data and I_0 were taken from the rutile powder diffraction file with entry 21-1276. The considered rutile reflections in the chosen 2θ range were (110), (101), (200), (111), (210), (211), (220) and (310).

3. Results

3.1. Coating microstructure and topography

In order to observe microstructure of the titania powder dispersed in suspension, it was dried for 2h at 150 ºC. The images presented in Fig. 1 shows substantial particle agglomeration. However, it is not clear whether such agglomeration occurs also in the readily sprayed suspension. The sizes of individual particles forming the agglomerate were in the range of 100 to 250 nm, and the average crystallite size determined from PXRD pattern was 154 ± 6 nm with the assumption of shape factor k = 0.89 commonly used for spherical crystallites. The size of the agglomerates from the laser diffractometry data corresponds well to the SEM images.

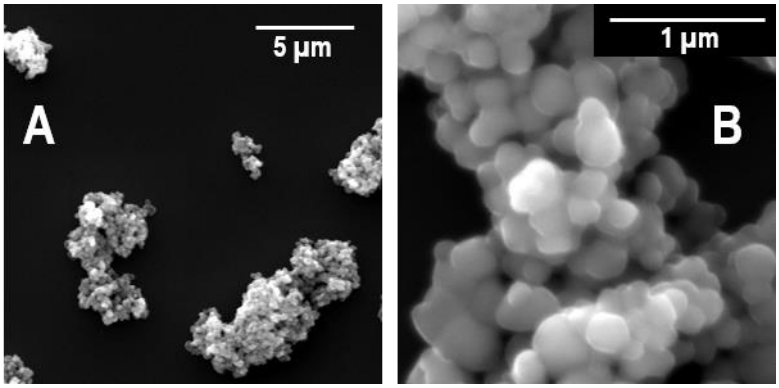

Fig. 1 Feedstock particles as observed in SE mode in SEM showing particle agglomeration (A) and the size of individual crystallites (B).

SE SEM images of the as-sprayed coating surfaces are shown in Fig. 2. The coatings can be divided into two groups according to the morphologies of the as-sprayed surfaces. The first group comprises coatings TG40 and TG56 sprayed with lower heat power, while the other group is comprised of the remaining coatings. For the lower heat power group, smooth coating surfaces were obtained as seen in Fig. 2, while the coatings sprayed with higher heat power have distinctive bulges or bumps on the as-sprayed surface. These bumps are mostly rounded in morphology and their size range is between 50-100 µm. These features are distributed uniformly over the entire top surface of the TG72, TG85 and TG101 coatings. Fig. 3 shows the SEM cross-section image of such a bump in coating TG 85. There are indications on the cross-sectional images that these bumps are associated with the creation of voids underneath them. It is clear that the bump appears as a cone-shaped structure with a void as the starting point. The void was formed during the spray run as a localised defect in the coating and no aggregates of unmolten particles was detected at the base of the cone. The void in the BSE image is around 15 µm. The clusters of porosity near their base were common to all the observed surface bumps. It was also noticed that the bumps have inter-pass porosities. No surface bumps were observed in TG40 and TG56 coatings. During thermal spraying, the surface roughness continually changes with each subsequent pass of the spray gun. The coating deposition begins with a relatively smooth grit blasted surface and the accumulation of individual splats as they are piled up in succession will alter the surface roughness for the next pass of the spray gun.

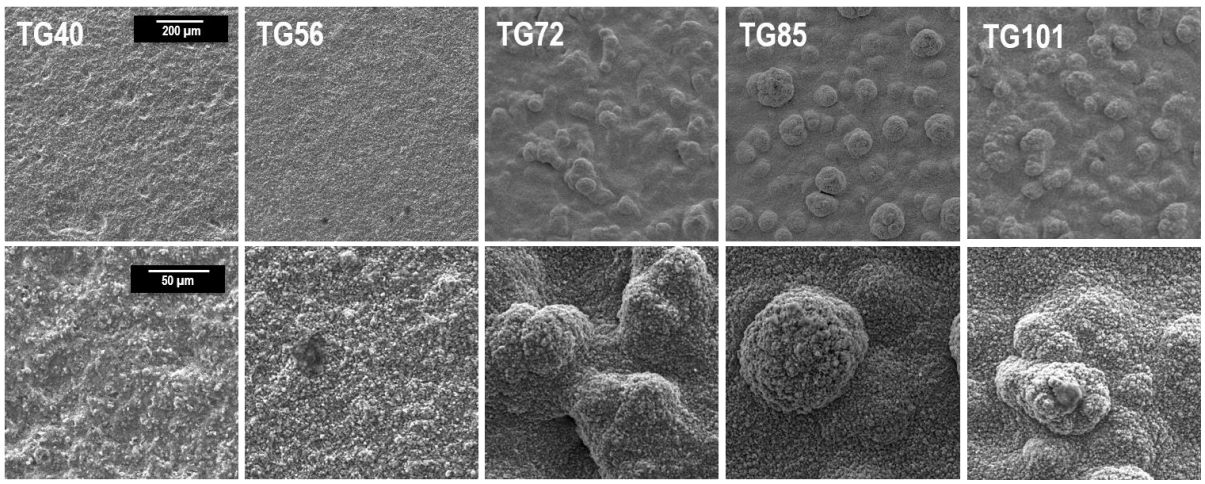

Fig. 2 Secondary electron images of the top surface morphologies of the as-sprayed surfaces; top row illustrates the emergence of humps in TG72, 85 and 101 with detailed features shown in bottom row.

Fig. 4 shows the detailed microstructure of the surface of coatings sprayed at low power flame (TG40) and coating sprayed at high flame power (TG85). The surface of the TG40 coating shows tiny agglomerated, sub-micron and nanosized particles resulting from unmelted or partially melted particles. When the suspension was sprayed with the low power spray conditions, a lower level of heat was transferred from the combustion flame to the particles, resulting in a higher amount of nano-sized particles retained from the suspension. Whereas, in the top surface of TG85 coating, the splats are mostly micron sized (with a small number of sub-micron splats) and they appear flattened due to the particle impact during deposition. The larger splat sizes indicate there was good heat transfer from the higher power combustion flame to the particles and the particles were in a molten state during impact. However, there are large inter-splat porosities present on the coating top surface.

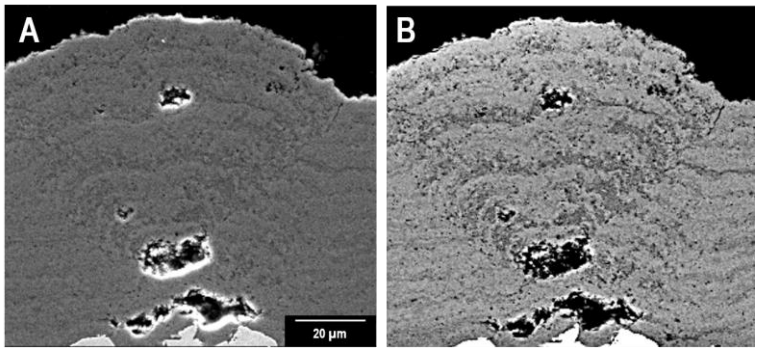

Fig. 3 Presence of voids underneath the bumps in TG85 coating observed in SE (A) and BSE (B) mode.

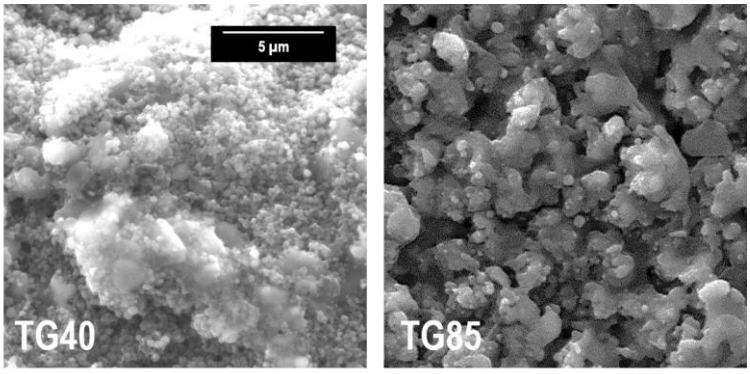

Fig. 4 SE images of the topography of as-sprayed TG40 and TG 85 coatings. Agglomeration of unmolten particles is observed in TG40 and the flattening of molten splats is noticeable in TG85.

The *Sp* and *Sa* height parameters from surface topography measurements and *Sdr* parameter are summarized in Fig. 5. Representative height maps for TG85 coating are shown in Fig. 6A,B. Closer scrutiny of height and area parameters reveals that the coatings can be divided into two groups with TG40 and TG56 comprising one and TG72, 85, 101 forming the other. Taking errors into account the maximum height of peaks *Sp* is the same for TG40 and TG 56, but increases monotonously with flame energy for the other group, approaching ~60 µm in TG101. The same behaviour is applicable to an overall parameter *Sa* which characterizes arithmetic mean height of the surface with monotonous increase with flame energy from 7.7 ± 0.3 µm to 9.6 ± 0.3 µm for the TG72, 85, 101.

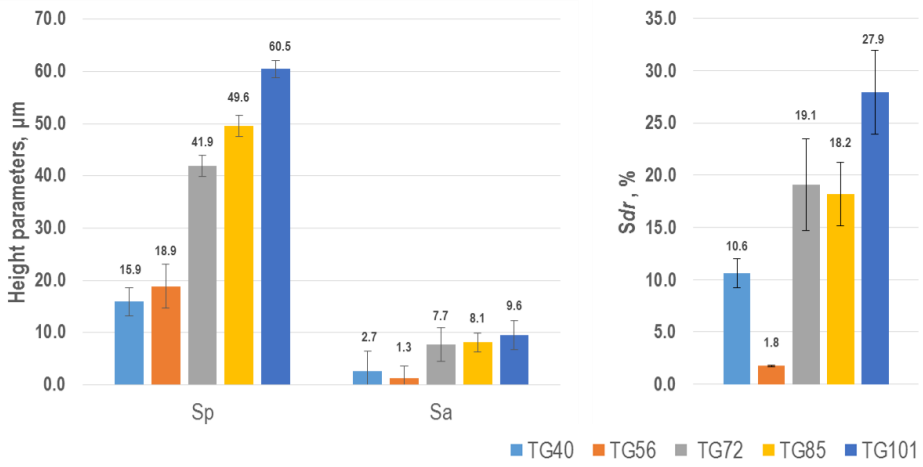

Fig. 5 Maximum height of peaks (*Sp*), arithmetical mean height of the surface (*Sa*) and surface area gain parameter *Sdr*.

The parameter Sdr, reflecting the gain in surface area with respect to the ideal flat plane, does not follow the same behaviour as Sp. In Fig. 4, the Sdr reaches about 10% for TG40, which is also the thinnest at 20 µm, and the impact of substrate grit-blasting will be more pronounced than in the other coatings. If only the TG56 to TG101 coatings are compared regarding the Sdr parameter, the gain in surface area is less than 2% for TG 56 and thus negligible, but reaches approximately 20% for TG72 and TG85 and 30 % for TG101. The comparatively large Sdr errors for TG72 to TG101 coatings reflects the fact that with higher magnification, the topography becomes more varied, meaning topography may change significantly between one image and the next one, leading to more significant variations of the Sdr parameter in the five regions it was sampled from. Higher magnification pictures from SEM in Fig. 2 testify to these variations in particular for the three coatings with humps. Whereas SEM pictures of the as-sprayed surface in Fig. 4 testify to submicrometric fine features, the surface topography results present a more macroscopic view that mirrors complex surface shapes of valleys and humps and the macroscopic gain in surface area due to their presence.

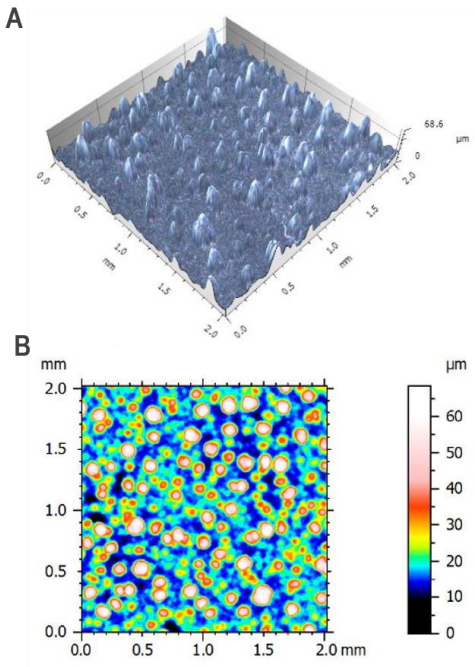

Fig. 6 Topography maps of a selected area on as-sprayed TG85 represented as a 3D surface (A) and as a 2D image (B).

The microstructures in the cross-sections (Fig. 7) demonstrate that titania coatings are well-bonded to the stainless steel substrate judging from the absence of cracks in the substrate/coating interface. In these coatings there were no horizontal cracks present, normally caused by cooling stresses in the coatings. These cracks are typically observed in titania sprayed at shorter stand-off distances. The coatings were also free from vertical cracks (except in TG 56), which suggests lower relaxation stresses in these coatings. In particular TG72, TG85 and TG101 have a layered microstructure which has already been reported for suspension HVOF sprayed titania coatings [9], [42].

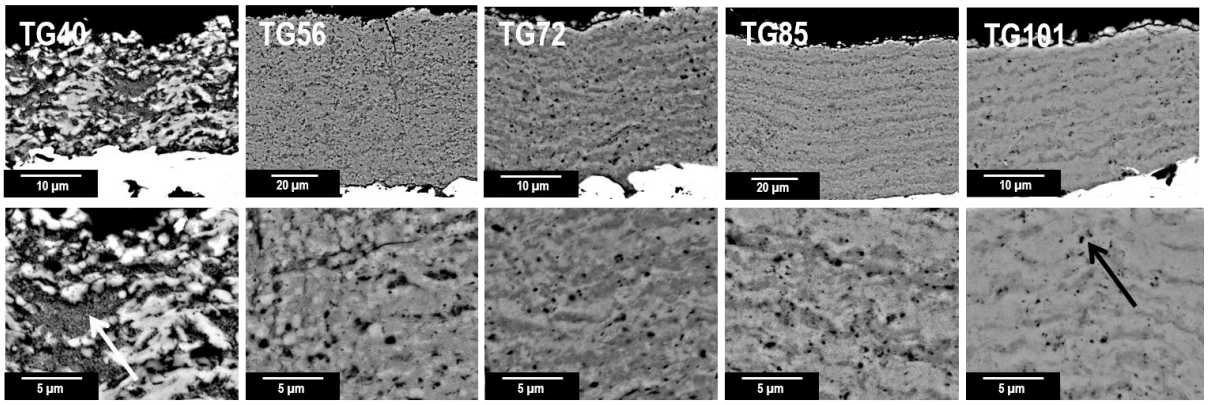

Fig. 7 BSE images of microstructures in cross-sections with pronounced particle agglomeration at lower energy (white arrow) and nanoscale porosity (black arrow). The occurrence of porosity especially at TG85 appears to be interpass in nature.

Since the contrast in BSE images is a function of mean atomic number, the brighter areas have higher average Z and as we can expect only titanium and oxygen atoms, the difference can be attributed either to a significant presence of vacancies or to the difference in Ti/O ratio in those regions. It should be noted that in rutile, atoms in the unit cell occupy less space than in anatase and, consequently, rutile has approximately 10% higher density. Thus we assume that the brighter regions correspond to rutile. The increase in volume fraction of the brighter regions with increasing heat power, corresponding to an increase in rutile/anatase ratio, is clearly visible in the lower row images of Fig. 7. The lower energy flame shows particle agglomeration especially for TG40 coatings, which is also the thinnest of all, namely 10 passes resulting in a ~20 µm thick coating. TG40 shows a bimodal coating microstructure which contains light grey structure with well-melted particles and dark grey structure of un-melted and agglomerated nanoparticles. As the combustion power increases these agglomerated nanoparticles decreased in the coatings due to better particle heating. The black areas on the coatings represent nanoscale porosity with TG101 coatings having clearly the lowest porosity among all; the decrease of porosity in titania thermally sprayed coatings with increasing power has already been documented [43]. As the total gas flow rate increases the gas velocity in SHVOF process also increases resulting in higher average particles velocities. It is well established that higher particle velocities result in lower porosity in the coatings and hence the degree of porosity gradually decreases from TG40 to TG101.

3.2. Phase composition and Rietveld refinement

The results presented in this section are representative for the volume irradiated during the PXRD experiment. Since the sizes of the slits were fixed, the measurement mode was "constant volume" when the irradiated surface area diminishes with increasing incident angle of primary X-ray beam, but the effective penetration depth increases in the scanned range from ~2 μm at 20° to ~7.5 μm at 90°.

PXRD patterns measured on the as-sprayed surfaces are compared with the dried powder pattern in Fig. 8 and document that the anatase to rutile transformation took place, which is commonly achieved during titania thermal spraying. The inset in Fig. 8 gives evidence about the decrease in intensity of (101) anatase reflection and increase of (110) rutile reflection intensity with higher heat power.

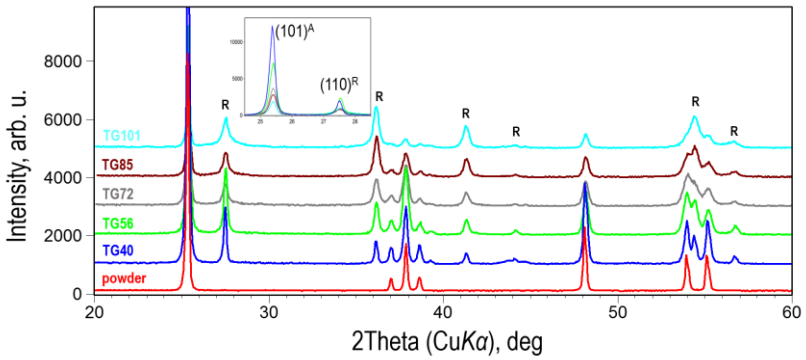

Fig. 8 PXRD patterns of powder and coatings with rutile reflections denoted by *R*, the unlabelled reflections are from anatase (powder pattern is pure anatase); the inset shows anatase and rutile reflections with intensity in absolute units.

Standard tetragonal structures of anatase and rutile were taken from the Inorganic Crystal Structure Database (ICSD) and used in Rietveld refinement. Only in the case of TG40 were other phases of titania detected by X-rays, namely weak reflections α-Fe and γ-Fe. This coating was thinner than 20 μm and, thus, X-rays penetrated also to the stainless steel substrate and the most diffracting $(111)^{\gamma}$ and $(110)^{\alpha}$ lines are observed in the fit of TG40 in Fig. 9. The quantities from Fig. 9 are compared in Tab. 3 with values obtained using eq. 1 and the RIR method. The issue of error calculation is a complex one for all three used approaches of quantitative phase analysis. In general only QRR gives error values,

which are relevant to the mathematical process of fitting the measured data [39] and not the general accuracy. The RIR values are given without errors in the PDF database and the intensities in equation (1) are also computed without errors. Thus only QRR values in Tab. 3 have errors.

Table. 3 Quantities and semi-quantity of anatase in wt.% according to 3 approaches.

Coating	**Rietveld refinement**	**Equation (1)**	**RIR**
TG40	79.9 ± 0.2	79	88
TG56	69.1 ± 0.3	63	78
TG72	58.8 ± 0.4	67	78
TG85	44.2 ± 0.4	55	67
TG101	20.5 ± 0.7	34	49

Regarding the first two rutile (110) and (101) reflections at ~27.5 and ~36 º2θ, their relative intensities should be 100% and 50% according to star quality PDF card no. 21-1276, but the intensity of (101) is higher than (110) for samples TG72, TG85 and TG101. Therefore, Lotgering factors were computed for these two reflections and are shown in Tab. 4.

Table. 4 Lotgering factors for (101), (110) and (211) rutile reflections calculated according to eq. (2).

Coating	**F(110)**	**F(101)**	**F(211)**
TG40	0.11	-0.01	-0.01
TG56	0.08	0.01	0.00
TG72	-0.22	0.11	0.07
TG85	-0.25	0.19	0.04
TG101	-0.22	0.15	0.02

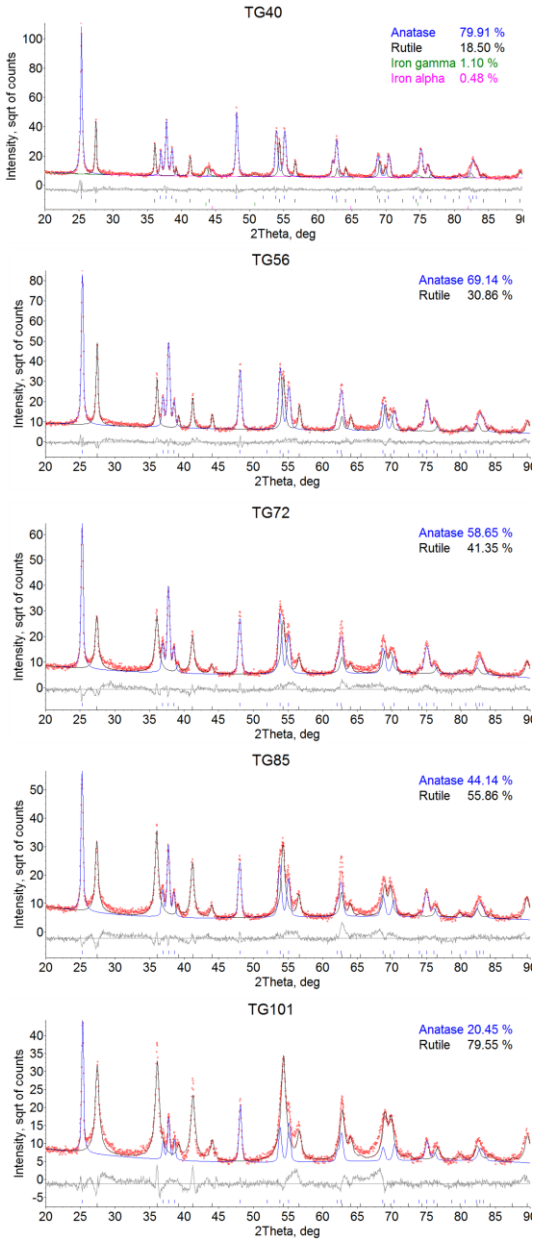

Fig. 9 Results of coatings PXRD patterns Rietveld refinement.

Considering the PXRD patterns from a profile analysis viewpoint, rutile reflections become broader as higher heat power is used for the coating's deposition. Since the crystallite size decreases with an increase in broadening, the average rutile crystallite is 85 ± 5 nm in the TG40 coating while it is 18 ± 1 nm in TG101. Average crystallite sizes of anatase and rutile in Fig. 10 show that TG72, TG85 and TG101 are similar with anatase having ~80 nm size crystallites across this range and rutile about 20 nm, and hencee crystallite sizes are not affected by flame energies on the higher energy level. Therefore, SHVOF spraying of ~150 nm anatase crystallites leads to coatings with even smaller

crystallites whose sizes can be controlled via energy of the flame. As the assumption of purely Lorentzian broadening due to small crystallites could be considered too stringent [44], we also attempted to refine crystallite sizes by simultaneous consideration of Lorentzian and Gaussian functions. In all cases, the improvement in fit was negligible and, more importantly, the change in calculated crystallite sizes and microstrains was virtually non-existent. The consideration of microstrain in rutile has not improved the structural fit in Rietveld refinements, but led to an appreciable improvement in the anatase case. All coatings except for TG40 have anatase with moderate microstrains exceeding 1×10^{-3}, or one milistrain, and the microstrain in rutile are either negligible or non-existent.

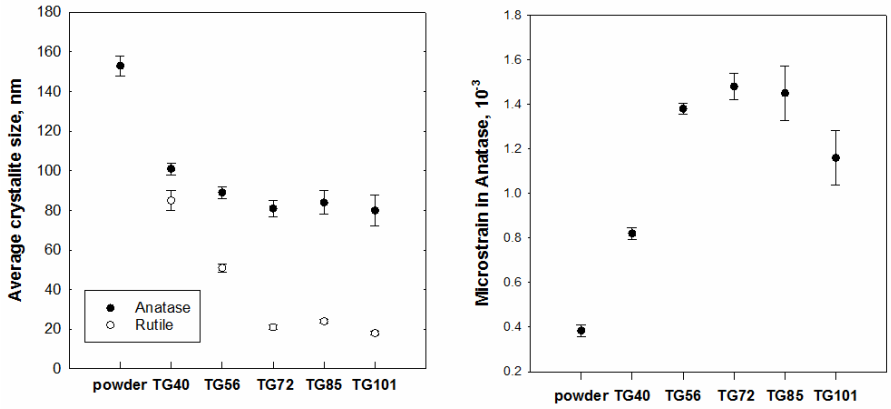

Fig. 10 Average crystallite sizes (D) and microstrain in anatase as obtained by Rietveld refinement.

4. Discussion

4.1. Quantitative phase composition

Selection of the most appropriate method for phase quantities calculation in the thermally sprayed coatings must be done with respect to the conditions which the particular method assumes on the state of the irradiated volume. In this paper, we have used three of the most common approaches [39] for evaluation of quantitative phase composition from PXRD data.

Both the RIR method and computations based on eq. 1 are dedicated to powder samples with the assumption of random orientation of powder particles which is, however, not fulfilled by the coatings analysed within the frame of this study. The simple preferred orientation characterization by Lotgering factors of selected rutile reflections in Tab. 4 reveals a certain degree of preferred orientation

of (110) planes in all the samples and of (101) planes in three coatings sprayed with higher energies. The negative values of *F(110)* for TG72, TG85 and TG101 coatings indicate that the measured intensity is less than in the randomly oriented sample [45]. On the other hand F(101), for the same three coatings, reach ~0.2 values which are virtually the same as reported for plasma sprayed TiO_2 coatings by Li and Ding [25] and reflect the existence of preferred orientation in these samples. Lotgering factors as such are a reliable method of validating preferred orientation in coatings, but by themselves cannot pinpoint relation between process parameters and texture. Nevertheless, these factors are useful when the applicability of the suitable method for phase quantity computation is to be verified. In particular, for quantitative phase composition in systems with two phases determined from classically measured intensities of diffraction profiles such as in eq. (1), the effect of texture is very strong and leads to substantial discrepancies between reality and obtained values [46].

In Rietveld refinement, two approaches can be used when the need arises to account for preferred orientation, either the so-called March-Dollase method [47] or employment of the spherical harmonics function as described in detail by Popa [48]. Upon performing the refinement, it becomes clear which reflections are not well matched in terms of intensity and for these reflections, the March-Dollase method can be applied to every phase in the irradiated volume considering up to two preferred orientation directions according to [49]. In order to get a significant improvement in the refined structural model, preferred orientation in anatase had to be considered for all coatings bar the ones with extreme amounts of anatase. Employment of March-Dollase method for rutile was necessary in the case of TG72, TG85 and TG101 coatings, using two preferred orientation directions of (101) and (111). Hence, it is suggested that quantitative Rietveld refinement is applied for phase quantity calculations in thermally sprayed coatings when Lotgering factors indicate presence of preferred orientation.

In general, rutile reflections become more intensive as higher heat power is used for the coating's deposition. This is mirrored by determined quantities listed in Tab. 3. While the normalized RIR method and eq. (1) take into account only one reflection from each anatase and rutile, the Hill and Howard algorithm incorporated in Rietveld refinement uses all reflections. Moreover, since the preferred orientation is present in agglomerates of rutile grains, only Rietveld refinement can take this

feature into account and is, thus, more accurate than the other two approaches and the quantities determined by QRR are considered in the following discussion.

4.2. Anatase to rutile transformation during SHVOF

Owing to the facts [10] that (i) rutile is the more stable TiO_2 phase at all temperatures and that (ii) the transformation rate from anatase to rutile is an exponential function of temperature, the increasing presence of rutile in coatings sprayed with a higher heat input is expected, and indeed, verified by the obtained results. With the aim of finding the relation between rutile quantity *R* and energy of the flame *E*, the five data points don't follow linear behaviour and are fitted better by a simple exponential function $R(E) = k1 \cdot e^{k2 \cdot E}$, with constants k1 = 7.74 and k2 = 0.02 and R-squared of 99.2%. Hence, within the number of coatings in this study, the rutile amount is an exponential function of heat input.

The anatase to rutile transformation during SHVOF leads to a distinctively layered coating microstructure seen in Fig. 7 where the areas with darker contrast correspond to occurrence of anatase whereas the lighter areas are rutile-rich. The existence of a time dependent temperature gradient during spraying is most likely the main driving force between the alternating presence of anatase and rutile in the layers, i.e. when a flame with higher energy and, thus, higher thermal input is used, the transformation to rutile is favoured.

Due to the spatial distribution of rutile and anatase crystallites, it is reasonable to expect a non-homogeneous field of macroscopic residual stresses, microstrains and possibly the crystallite sizes also follow a certain pattern within the coatings. Lacking the beam size necessary for such detailed analysis, we nevertheless attempted line profile analysis [50] aimed at determination of average microstrains and average crystallite sizes (or coherently scattering domains) whose results are presented in Fig. 10. For three higher heat powers, the crystallite sizes barely change whereas the anatase quantity decreases from 60 to 20 wt.%. It is therefore possible that the mechanism of critical titania particle size, similar to the one proposed by Reidy et al. [24], is also in play during SHVOF process. As for microstrains, their larger values in anatase as compared with rutile bear similarities to the findings in titania nanopowders, in which anatase is expected to have larger microstrains [51].

Another important feature of SHVOF spraying of titania is the production of a particular coating surface topography with an array of humps for higher energies of 72, 85 and 101 kW as seen in Figs. 2, 3 and, in particular, Fig. 6. The humps bear resemblance to the so called cauliflower or broccoli surface morphologies [52] obtained during suspension plasma spraying of yttria stabilized zirconia or alumina. However, the columnar structure usually associated with the cauliflower/ broccoli morphology was not observed in the coatings here and, instead, creation of voids took place. Analysis of small particle plasma sprayed alumina coatings by Trice and Faber [53] documented formation of similar humps. The formation of humps was attributed to small perturbations developed from splashing and subsequent impact of melted particles, which were divided by the perturbations, leading to formation of porosity on the boundaries between the hump area and the surrounding environment (for detailed explanation see Fig. 9 in [53]). While the authors sprayed nominally 9 μm sized alumina particles, we sprayed much smaller particles from suspension. On the other hand, Stiegler et al. in a study of suspension HVOF sprayed hydroxyapatite coating [54] reported the formation of humps in their coatings and attributed these to the aggregates of unmolten particles at the base of the humps. In theory, both mechanisms can be responsible for the formation of humps observed in our study. It is clear from the cross-sections in this study that the base of all the humps have either voids ranging from ~5-15 μm or surface irregularities caused by grit blasting of the substrate. The smaller particles used in this experiment can easily replicate the surface anomalies of the grit blasted surface resulting in cone shaped structure. Now moving onto the voids at the base of the cone, these voids or porosities can be easily created due to insufficient bonding of particles during the layer to layer deposition. Another hypothesis is that a large aggregate of unmolten particles created a surface asperity and the incoming molten splats was divided into several segments upon impacting the asperity. This poorly bonded large aggregate of unmolten particles can be successively removed by incoming hot gas jet from the gun. Once a defect is formed the growth of the cone relies on successive particle deposition which exaggerates the defect. The smaller particles in SHVOF tend to follow the gas flow characteristics due to their low inertia. In addition, the smaller particles in SHVOF have lower Stokes numbers and a lower Stokes number indicates the smaller particle can be affected by the turbulent flow due to the presence of the substrate and deflected.

The deflected particle having velocity component parallel to the substrate can stick to the asperities and subsequent preferential growth of the humps.

Hence we can expect substantial gains in surface area when TiO_2 coatings are prepared via the SHVOF route employing higher heat powers of the flame, which has been confirmed by topographical measurements with the *Sdr* parameter pointing to ~30 % macroscopic area gain in TG101. The higher surface area and asperities may prove beneficial in applications where a larger surface area is required.

5. Conclusions

SHVOF spraying of water based suspension from ~180 nm anatase particles leads to coatings with duplex anatase/rutile composition which can be tuned by spraying parameters; an increase in flame power leads to more rutile in the coating. It was found that within the frame of the number of analysed coatings, the rutile amount in the coatings is an exponential function of heat input of the flame.

It is suggested that preferably quantitative Rietveld refinement is used for quantitative phase analysis in titania thermally sprayed coatings, because the technique can take into account the existence of preferred orientation originating due to the inherent anisotropy of the deposition process. Higher flame power, i.e. corresponding to 72, 85 and 101 kW, does not affect the crystallite size of anatase (~80 nm) and rutile (~20 nm). Also, spraying with higher power leads to the presence of microstrains in anatase of 10^{-3} magnitude; whereas, microstrains in rutile are either negligible or non-existent. Origination of rutile is connected with emergence of preferred orientation and, thus, the rutile crystallites are not randomly oriented in the coating.

Coatings sprayed with lower energies have relatively smooth as-sprayed surfaces while for higher energies (72 kW and above), typically humps are seen on the surface. The formation of these humps was associated with surface irregularities at the base of the cone shaped features. The emergence of these humps lead to a substantial increase of surface area of the TiO_2 coating and added about 30 % area with respect to the ideally flat coating when the highest heat power of the flame was used.

Acknowledgements

The work was funded by the Engineering Research Placement (ERP) scheme at the Faculty of Engineering. E. Shaw acknowledges support from Bombardier Transportation UK Ltd, Z. Pala acknowledges support from USC-CFB-CMM project and N. Senin acknowledges support of EU-FP7-MC IEF – METROSURF project. A kind assistance of Rory Screaton during the spraying process is gratefully acknowledged. Authors also wish to thank prof. Radomir Kuzel from Charles University for fruitful discussion regarding line profile analysis.

References

[1] L. Pawlowski, "Finely grained nanometric and submicrometric coatings by thermal spraying: A review," *Surf. Coatings Technol.*, vol. 202, no. 18, pp. 4318–4328, 2008.

[2] J. O. Berghaus, J.-G. Legoux, C. Moreau, F. Tarasi, and T. Chráska, "Mechanical and thermal transport properties of suspension thermal-sprayed alumina-zirconia composite coatings," *J. Therm. Spray Technol.*, vol. 17, no. 1, pp. 91–104, 2008.

[3] F.-L. Toma, L.-M. Berger, T. Naumann, and S. Langner, "Microstructures of nanostructured ceramic coatings obtained by suspension thermal spraying," *Surf. Coatings Technol.*, vol. 202, no. 18, pp. 4343–4348, 2008.

[4] P. Fauchais, M. Vardelle, A. Vardelle, and S. Goutier, "What Do We Know, What are the Current Limitations of Suspension Plasma Spraying?," *J. Therm. Spray Technol.*, vol. 24, no. 7, pp. 1120–1129, 2015.

[5] M. Gardon and J. M. Guilemany, "Milestones in Functional Titanium Dioxide Thermal Spray Coatings : A Review," *J. Therm. spray Technol.*, vol. 23, no. April, pp. 577–595, 2014.

[6] S. Kozerski, F. Toma, L. Pawlowski, B. Leupolt, L. Latka, and L. Berger, "Suspension plasma sprayed TiO2 coatings using different injectors and their photocatalytic properties," *Surf. Coat. Technol.*, vol. 205, no. 4, pp. 980–986, 2010.

[7] R. Jaworski, L. Pawlowski, F. Roudet, S. Kozerski, F. Roudet, and S. Kozerski, "Influence of Suspension Plasma Spraying Process Parameters on TiO 2 Coatings Microstructure," *J. Therm. spray Technol.*, vol. 17, no. March, pp. 73–81, 2008.

[8] E. Rayón, V. Bonache, M. D. Salvador, E. Bannier, E. Sánchez, A. Denoirjean, and H. Ageorges, "Nanoindentation study of the mechanical and damage behaviour of suspension plasma sprayed TiO2 coatings," *Surf. Coat. Technol.*, vol. 206, no. 10, pp. 2655–2660, 2012.

[9] G. Bolelli, V. Cannillo, R. Gadow, A. Killinger, L. Lusvarghi, and J. Rauch, "Properties of High Velocity Suspension Flame Sprayed (HVSFS) TiO2 coatings," *Surf. Coat. Technol.*, vol. 203, no. 12, pp. 1722–1732, 2009.

[10] D. A. H. Hanaor and C. C. Sorrell, "Review of the anatase to rutile phase transformation," *J. Mater. Sci.*, vol. 46, no. 4, pp. 855–874, 2011.

[11] J. Augustynski, "The role of the surface intermediates in the photoelectrochemical behaviour of anatase and rutile TiO 2," *Electrochim. Acta*, vol. 38, no. 1, pp. 43–46, 1993.

[12] Y. Hu, H.-L. Tsai, and C.-L. Huang, "Effect of brookite phase on the anatase–rutile transition in titania nanoparticles," *J. Eur. Ceram. Soc.*, vol. 23, no. 5, pp. 691–696, Apr. 2003.

[13] D. C. Hurum, A. G. Agrios, K. A. Gray, T. Rajh, and M. C. Thurnauer, "Explaining the enhanced photocatalytic activity of Degussa P25 mixed-phase TiO2 using EPR," *J. Phys. Chem. B*, vol. 107, no. 19, pp. 4545–4549, 2003.

[14] J. C. Yu, L. Zhang, and J. Yu, “Direct Sonochemical Preparation and Characterization of Highly Active Mesoporous TiO 2 with a Bicrystalline Framework,” *Chem. Mater.*, no. 11, pp. 4647–4653, 2002.

[15] H. Xu and L. Zhang, “Controllable One-Pot Synthesis and Enhanced Photocatalytic Activity of Mixed-Phase TiO 2 Nanocrystals with Tunable Brookite / Rutile Ratios,” *J. Phys. Chem. C*, vol. 113, pp. 1785–1790, 2009.

[16] M. Kaneko and I. Okura, *Photocatalysis, Science and Technology*. Kodansha Springer, 2002.

[17] W. A. Daoud, *Self-cleaning materials and surfaces: a nanotechnology approach*. John Wiley & Sons, 2013.

[18] A. L. Linsebigler, G. Lu, and J. T. Yates, “Photocatalysis on TiO2 Surfaces: Principles, Mechanisms, and Selected Results,” *Chem. Rev.*, vol. 95, no. 3, pp. 735–758, 1995.

[19] S. J. Han, H. Lee, Z. Pala, and S. Sampath, “Tunability of Thermoelectric Properties of in situ Thermal Spray Synthesized TiO2-x,” *Prep.*

[20] S. Andersson, B. Collén, U. Kuylenstierna, and A. Magnéli, “Phase Analysis Studies on the Titanium-Oxygen System,” *Acta Chem. Scand.*, vol. 11, pp. 1641–1652, 1957.

[21] N. Okinaka and T. Akiyama, “Latent property of defect-controlled metal oxide: nonstoichiometric titanium oxides as prospective material for high-temperature thermoelectric conversion,” *Jpn. J. Appl. Phys.*, vol. 45, no. 9R, p. 7009, 2006.

[22] N. Berger-Keller, G. Bertrand, C. Filiatre, C. Meunier, and C. Coddet, “Microstructure of plasma-sprayed titania coatings deposited from spray- dried powder,” *Surf. Coatings Technol.*, vol. 168, no. 03, pp. 281–290, 2003.

[23] A. Ohmori, H. Shoyama, S. Matsusaka, K. Ohashi, K. Moriya, K. Moriya, and C. J. Li, “Study of photo-catalytic character of plasma sprayed TiO sub 2 coatings,” in *ITSC 2000: 1 st International Thermal Spray Conference*, 2000, pp. 317–323.

[24] D. J. Reidy, J. D. Holmes, and M. A. Morris, “The critical size mechanism for the anatase to rutile transformation in TiO2 and doped-TiO2,” *J. Eur. Ceram. Soc.*, vol. 26, no. 9, pp. 1527–1534, 2006.

[25] J. F. Li, C. X. Ding, and others, “Crystalline orientation of plasma-sprayed TiO2 coatings,” *J. Mater. Sci. Lett.*, vol. 17, no. 20, pp. 1747–1749, 1998.

[26] G. Tian, H. Fu, L. Jing, B. Xin, and K. Pan, “Preparation and characterization of stable biphase TiO2 photocatalyst with high crystallinity, large surface area, and enhanced photoactivity,” *J. Phys. Chem. C*, vol. 112, no. 8, pp. 3083–3089, 2008.

[27] J. C. Yu, J. Yu, W. Ho, Z. Jiang, and L. Zhang, “Effects of F - Doping on the Photocatalytic Activity and Microstructures of Nanocrystalline TiO 2 Powders,” *Chem. Mater.*, no. 14, pp. 3808–3816, 2002.

[28] S. Brunauer, P. H. Emmett, and E. Teller, “Adsorption of Gases in Multimolecular Layers,” *J. Am. Chem. Soc.*, vol. 60, no. 2, pp. 309–319, 1938.

[29] B. Jenny and P. Pichat, “Determination of the actual photocatalytic rate of hydrogen peroxide decomposition over suspended titania. Fitting to the Langmuir-Hinshelwood form,” *Langmuir*, vol. 7, no. 5, pp. 947–954, 1991.

[30] Y. Xu and C. H. Langford, “UV- or Visible-Light-Induced Degradation of X3B on TiO 2 Nanoparticles : The Influence of Adsorption,” *Langmuir*, no. 12, pp. 897–902, 2001.

[31] H. M. Rietveld, “Line profiles of neutron powder-diffraction peaks for structure refinement,” *Acta Crystallogr.*, vol. 22, no. 1, pp. 151–152, 1967.

[32] R. J. Hill and C. J. Howard, “Quantitative phase analysis from neutron powder diffraction data using the Rietveld method,” *J. Appl. Crystallogr.*, vol. 20, no. 6, pp. 467–474, Dec. 1987.

[33] P. Scardi and M. Leoni, “Whole powder pattern modelling,” *Acta Crystallogr. Sect. A Found.*

Crystallogr., vol. 58, no. 2, pp. 190–200, Feb. 2002.

[34] "ISO 25178-2:2012 Geometrical product specifications (GPS) -- Surface texture: Areal -- Part 2: Terms, definitions and surface texture parameters." .

[35] L. B. Mccusker, R. B. Von Dreele, D. E. Cox, D. Louër, and P. Scardi, "Rietveld refinement guidelines," *J. Appl. Crystallogr.*, vol. 32, no. 1, pp. 36–50, 1999.

[36] M. A. Tagliente and M. Massaro, "Strain-driven (002) preferred orientation of ZnO nanoparticles in ion-implanted silica," *Nucl. Instruments Methods Phys. Res. Sect. B Beam Interact. with Mater. Atoms*, vol. 266, no. 7, pp. 1055–1061, 2008.

[37] P. Scardi, M. Leoni, and R. Delhez, "Line broadening analysis using integral breadth methods : a critical review research papers," *J. Appl. Crystallogr.*, vol. 37, no. 1, pp. 381–390, 2004.

[38] R. W. Cheary, A. A. Coelho, and J. P. Cline, "Fundamental parameters line profile fitting in laboratory diffractometers," *J. Res. Inst. Stand. Technol.*, vol. 109, pp. 1–26, 2004.

[39] I. C. Madsen, N. V Scarlett, L. M. Cranswick, and T. Twin, "Outcomes of the International Union of Crystallography Commission on Powder Diffraction Round Robin on Quantitative Phase Analysis : samples 1 a to 1 h," *J. Appl. Crystallogr.*, vol. 34, no. 1, pp. 409–426, 2001.

[40] F. H. Chung, "Quantitative interpretation of X-ray diffraction patterns of mixtures. I. Matrix-flushing method for quantitative multicomponent analysis," *J. Appl. Crystallogr.*, vol. 7, no. 6, pp. 519–525, 1974.

[41] F. K. Lotgering, "Topotactical reactions with ferrimagnetic oxides having hexagonal crystal structures—I," *J. Inorg. Nucl. Chem.*, vol. 9, no. 2, pp. 113–123, Feb. 1959.

[42] E. Bemporad, G. Bolelli, V. Cannillo, D. De Felicis, R. Gadow, A. Killinger, L. Lusvarghi, J. Rauch, and M. Sebastiani, "Structural characterisation of High Velocity Suspension Flame Sprayed (HVSFS) TiO2 coatings," *Surf. Coat. Technol.*, vol. 204, no. 23, pp. 3902–3910, 2010.

[43] P. Ctibor and M. Hrabovsky, "Plasma sprayed TiO2: The influence of power of an electric supply on particle parameters in the flight and character of sprayed coating," *J. Eur. Ceram. Soc.*, vol. 30, no. 15, pp. 3131–3136, 2010.

[44] D. Balzar, N. Audebrand, M. Daymond, A. Fitch, A. Hewat, J. Langford, A. Le Bail, D. Louër, O. Masson, C. McCowan, N. Popa, P. Stephens, and B. H. Toby, "Size – strain line-broadening analysis of the ceria round-robin sample," *J. Appl. Crystallogr.*, vol. 37, pp. 911–924, 2004.

[45] R. J. Ong, D. A. Payne, and N. R. Sottos, "Processing effects for integrated PZT: Residual stress, thickness, and dielectric properties," *J. Am. Ceram. Soc.*, vol. 88, no. 10, pp. 2839–2847, 2005.

[46] J. T. Bonarski, M. Wróbel, and K. Pawlik, "Quantitative phase analysis of duplex stainless steel using incomplete pole figures," *Mater. Sci. Technol.*, vol. 16, no. 6, pp. 657–662, 2000.

[47] W. A. Dollase, "Correction of Intensities for Preferred Orientation in Powder Diffractometry : Application of the March Model," *J. Appl. Cryst.*, vol. 19, pp. 267–272, 1986.

[48] N. C. Popa, "Texture in Rietveld refinement," *J. Appl. Crystallogr.*, vol. 25, no. 5, pp. 611–616, 1992.

[49] A. March, "Mathematische Theorie der Regelung nach der Korngestah bei affiner Deformation," *Zeitschrift für Krist. Mater.*, vol. 81, no. 1–6, pp. 285–297, 1932.

[50] R. Delhez, T. H. De Keijser, and E. J. Mittemeijer, "Determination of crystallite size and lattice distortions through X-ray diffraction line profile analysis," *Fresenius' Zeitschrift für Anal. Chemie*, vol. 312, no. 1, pp. 1–16, 1982.

[51] L. E. Depero, L. Sangaletti, B. Allieri, E. Bontempi, A. Marino, and M. Zocchi, "Correlation between crystallite sizes and microstrains in TiO 2 nanopowders," *J. Cryst. Growth*, vol. 198, pp. 516–520, 1999.

[52] F.-L. Toma, G. Bertrand, D. Klein, C. Coddet, and C. Meunier, “Nanostructured photocatalytic titania coatings formed by suspension plasma spraying,” *J. Therm. spray Technol.*, vol. 15, no. 4, pp. 587–592, 2006.

[53] R. W. Trice and K. T. Faber, “Role of Lamellae Morphology on the Microstructural Development and Mechanical Properties of Small-Particle Plasma-Sprayed Alumina,” *J. Am. Ceram. Soc.*, vol. 83, no. 4, pp. 889–896, 2000.

[54] N. Stiegler, D. Bellucci, G. Bolelli, V. Cannillo, R. Gadow, A. Killinger, L. Lusvarghi, and A. Sola, “High-velocity suspension flame sprayed (HVSFS) hydroxyapatite coatings for biomedical applications,” *J. Therm. spray Technol.*, vol. 21, no. 2, pp. 275–287, 2012.